

Kinemon: An inductively shunted transmon artificial atom

Daria Kalacheva^{1,2,3,*}, Gleb Fedorov^{1,2,3,4}, Julia Zotova^{1,2,3}, Shamil Kadyrmetov^{1,2},
Alexey Kirkovskii^{1,2}, Aleksei Dmitriev^{1,2}, and Oleg Astafiev^{1,2}

¹Skolkovo Institute of Science and Technology, Skolkovo Innovation Center, Moscow 121205, Russia

²Moscow Institute of Physics and Technology, 9 Institutsky Lane, Dolgoprudny 141700, Russia

³National University of Science and Technology MISIS, 119049 Moscow, Russia

⁴Russian Quantum Center, National University of Science and Technology MISIS, 119049 Moscow, Russia

(Received 21 June 2023; revised 5 February 2024; accepted 7 February 2024; published 29 February 2024)

We experimentally investigate inductively shunted transmon-type artificial atoms as an alternative to address the challenges of low anharmonicity and the need for strong charge dispersion in superconducting quantum systems. We characterize several devices with varying geometries and parameters (Josephson energies and capacitances), and find a good agreement with calculations. Our approach allows us to retain the benefits of transmon qubit engineering and fabrication technology and high coherence, while potentially increasing anharmonicity. The approach offers an alternative platform for the development of scalable multiqubit systems in quantum computing.

DOI: 10.1103/PhysRevApplied.21.024058

Superconducting artificial quantum systems, such as the capacitively shunted charge qubits (transmons and Xmons) are now commonly used to build prototypes of quantum processors because of their simple design and low decoherence rates [1–4]. However, scaling up quantum registers composed of low anharmonicity physical qubits faces challenges due to the uncontrolled transitions to upper states and limitations in speed of quantum operations [5–10]. Additionally, non-negligible charge dispersion of the higher-energy levels complicates the use of such artificial atoms as qudits [11]. These problems drive the search for alternative physical qubits and materials [12–16].

While retaining simplicity in fabrication and operation, together with charge-noise insensitivity, one can increase the nonlinearity of a transmon by decreasing its shunting capacitance and, at the same time, shunting it by a linear inductance. Strictly speaking, this modification produces a flux qubit [17–21], more specifically, an rf superconducting quantum interference device (SQUID) or a fluxonium [22]; however, its parameters can be chosen so that the resulting eigenstates are transmonlike, living in a single-well potential, not a two-well one. The latter helps to avoid the exponential sensitivity of the transition frequencies to the Josephson energy variations, which has so far limited the applications of flux qubits in multiqubit devices. Also, one can expect that the inductive shunt will remove charge dispersion for arbitrarily high-energy states.

In this study, we explore an alternative hybrid design combining the transmon circuit with a compact kinetic inductor—a kinemon (kinetic-inductance-shunted transmon) artificial atom (Fig. 1). We design and investigate experimentally a family of such systems with various combinations of Josephson energy E_J , inductive energy E_L , and charging energy E_C [3]. Our current values fall in the area between the transmon and the CPB in terms of the ratio E_J/E_C . Concerning the inductive energy, we use a small inductance ($E_J/E_L \leq 1$), moving closer to a linear LC circuit; however, the system is still anharmonic enough and resembles the transmon or a quarton [24]. The kinemon spectrum is strongly dependent on the magnetic flux, i.e., its anharmonicity can change the sign when the system is tuned between its flux sweet spots. We also show that the inductive element can be placed inside an α SQUID [26], which, for a correct ratio of resulting loop areas, opens a way to modulate the effective Josephson energy, while keeping the parabolic potential contribution fixed. Such double-loop kinemons (group B in Fig. 2) cannot be unambiguously represented by a single point on the diagram in Fig. 1.

Of note, we find that, confirming our previous tests of coplanar resonators [27], the kinetic inductor based on aluminum ultra-thin-film does not cause any noticeable deterioration of the coherence times. Finally, as this kind of inductor exhibits relatively good reproducibility in fabrication, we find it a promising component for future quantum circuits.

Without the inductive shunt, a Josephson junction is characterized by a periodic potential $U_J = -E_J \cos \varphi$,

*d.kalacheva@gmail.com

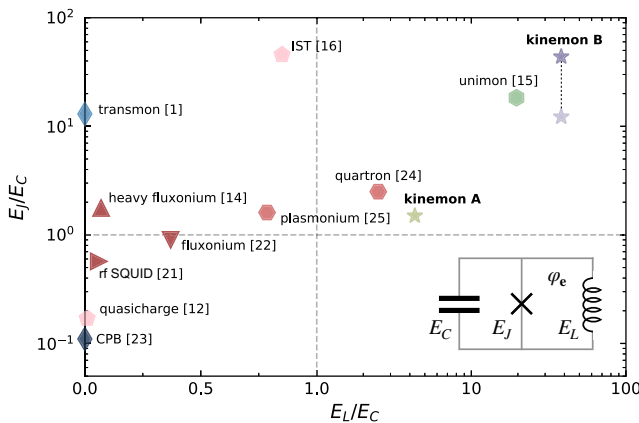


FIG. 1. The parameter space for various superconducting qubits is depicted through an equivalent three-element circuit model, as shown in the inset. The Josephson energy (E_J) and inductive energy (E_L) are contrasted with the charging energy ($E_C = 2e^2/C$). The green and violet stars represent two types of kinemon artificial atoms introduced in this work. Additional experimental data are cited from Refs. [1,12,14–16,21–25].

where φ is the phase across the junction [Fig. 2(a)]. Adding a small parallel capacitance to the circuit results in the formation of energy bands of Bloch waves in the periodic potential [28], which can be represented as $\psi'(\varphi) = e^{i(q'/2e)\varphi}\psi(\varphi)$, so that $\psi'(\varphi) \neq \psi'(\varphi + 2\pi)$ and

only $u(\varphi) = u(\varphi + 2\pi)$. Here, q' represents the quasicharge, being the analogue of the crystal momentum in solids, and the energies inside the band are periodic functions of q' . We note that for a charge qubit with discrete number of Cooper pairs allowed on the island, we can apply the rotor analogy [1,29], so that the states after a full rotation are indistinguishable. Then, the wave function is 2π -periodic in the φ representation, and the bands seem to disappear. However, as there is a mathematical correspondence between the quasicharge q' and the induced charge n_g : $n_g = q'/2e$, the energy configuration of the system still exhibits the same oscillatory behavior as a function of n_g . While a larger capacitance localizes the lower-energy states in distinct potential wells and significantly reduces the widths of the lowest bands, higher-lying bands remain open, as shown in Fig. 2(a), and thus are still sensitive to the induced charge. Moreover, increasing the capacitance always comes at the cost of reducing the anharmonicity α [1].

To completely prevent the formation of energy bands (remove any energy dependence on the induced charge n_g), it is necessary to disrupt the periodicity. This can be achieved by implementing a shunting inductance, which introduces a parabolic potential $U_L = E_L\varphi^2/2$ to U_J as exemplified in Fig. 2(a). As a result, the wave functions of the lowest states become localized in the central well. Note that in the case of a small E_L ($\leq E_J$), the anharmonicity and the energy structure are predominantly determined by

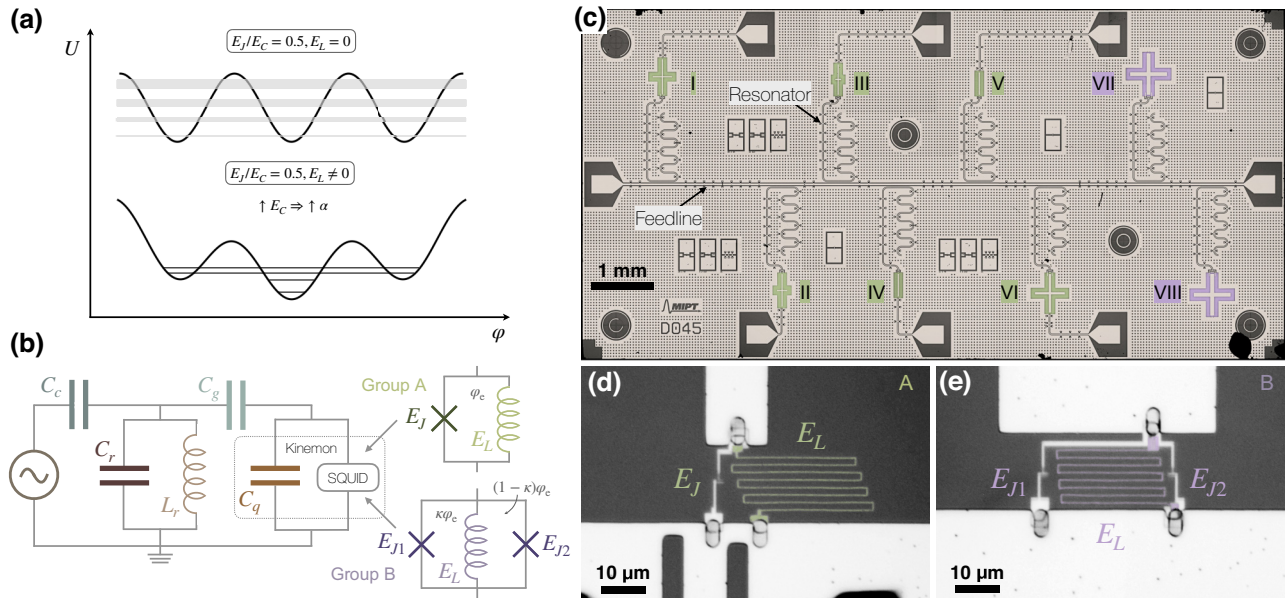


FIG. 2. (a) The potential (solid black line) and the energy levels (gray lines) for the conventional transmon (top) and for the inductively shunted one (bottom) for $q_e = 0$. (b) Circuit model of the sample. SQUIDs consists of Josephson junction and a kinetic wire with the energies E_J and E_L , respectively, and are shunted by a large capacitance with an energy E_C forming a kinemon atom. Group A (green color) represents asymmetric kinemons with different energy ratios (kinemons I–VI). Group B (violet color) represents symmetric kinemons with two JJs and a kinetic inductance wire between them (kinemons VII–VIII). (c) Overview optical image of the fabricated sample. Microfabrication design includes two groups of art. atoms with different topologies and variations of E_C , E_L , and E_J . (d),(e) Enlarged optical image of two different kinemon modification.

E_J and E_C . This is because the Josephson energy E_J governs the energy landscape of the system, with the smaller inductive energy E_L providing only a minor perturbation. Larger E_L/E_J results in less anharmonicity but can be compensated by increasing E_C . In the present work, though, we study inductively shunted artificial atoms fabricated using the standard transmon technology ($E_C \ll E_J \lesssim E_L$) and aim to verify their properties and coherence.

A schematic equivalent circuit of kinemon artificial atom is depicted in Fig. 2(b), illustrating two different configurations of qubits investigated in this work. Qubits consist of two main parts: Al/AlO_x/Al Josephson junctions and a kinetic inductance wire with energy $E_L = \Phi_0^2/4\pi^2L_k$ due to the wire inductance L_k to form a SQUID loop. The first circuit scheme operates with an asymmetric topology, utilizing a small single loop formed by an aluminum wire interrupted by a single Josephson junction [group A in Fig. 2(b)]. A key characteristic of this mode is the variation of shunting capacitance values ($E_C = 2e^2/C$) to examine coherence time. The second circuit scheme employs a symmetric topology that merges the benefits of both rf SQUID and transmon designs [group B in Fig. 2(b)]. This approach aims to enhance qubit performance by incorporating a double-loop architecture connected by a shared kinetic inductance wire.

The common Hamiltonian, which covers both the considered geometries (single- and double-loop circuits), can be expressed as follows:

$$\hat{\mathcal{H}} = -E_C \frac{\partial^2}{\partial \varphi^2} + \frac{1}{2} E_L \varphi^2 - E_{J1} \cos(\varphi + \kappa \varphi_e) - E_{J2} \cos(\varphi - (1 - \kappa)\varphi_e), \quad (1)$$

where φ_e is the total flux phase induced by an external magnetic field, κ is the coefficient of φ_e distribution between two loops, E_{J1} and E_{J2} are the Josephson energies of the junctions in each loop according to Fig. 2(b). The Hamiltonian for group A is obtained by putting $E_{J2} = 0$.

An optical image of the sample is presented in Fig. 2(c), depicting the microfabricated superconducting circuit containing eight kinemon artificial atoms. SQUIDs are tiny loops of superconducting wire and Josephson junctions connected to other circuit elements, such as capacitors and resonators. The SQUIDs are highlighted in green and violet false colors depending on their architecture, Figs. 2(d) and 2(e).

The fabrication of the kinetic inductance wire is done as follows. A silicon substrate is cooled down by liquid nitrogen during metal deposition to obtain uniform films up to 3.5 nm thick. It is known that aluminum films, deposited at room temperature are negatively impacted by formation of granules. Cold-film deposition allows us to fabricate long ultrathin wires with a high degree of homogeneity [27]. The detailed fabrication process is described in Appendix B. To achieve the necessary inductive energy

E_L , 200-nm-wide and 8-nm-thick aluminum wires with varying lengths are integrated into the circuit. Since the kinetic inductance per square of such a film is about 0.03 nH/◻, the wire length in the device ranges from 80 to 240 μm, depending on the desired E_L .

In Fig. 3(a) top, we display the data of transmission spectroscopy of the sample via the feedline, showing the microwave response of the readout resonator I as a function of the flux bias φ_e through the SQUID of kinemon I (group A). See all resonators' spectra in Fig. 7 in Appendix E. The pattern is a combination of a smooth dependence, formed by the kinemon first excited state located below the resonator frequency, and an avoided crossing pattern with the second excited state [30]. Direct observation of these transitions is enabled by the cross-Kerr dispersive spectroscopy, for which the data are displayed in Fig. 3(a) bottom. The minimum frequency (one-half flux quantum) and the maximum frequency (zero flux) are considered the flux “sweet spots.” Figure 3(a) bottom, also presents the fits to the experimental transition frequencies based on the circuit Hamiltonian [Eq. (1)]. The fits align well with the experimental transition frequencies near the sweet spots $\varphi_e = 0$ and $\varphi_e = \pi$. The single-photon transition between the ground $|0\rangle$ and excited $|1\rangle$ states occurs at $f_{01} = 4.947$ GHz at $\varphi_e = 0$. Furthermore, the bottom sweet spot of the transition from $|0\rangle$ to $|2\rangle$ is at $f_{02} = 5.6$ GHz and not visible at $\varphi_e = \pi$ and corresponds to anticrossings in the transmission spectroscopy. However, the two-photon transition can be observed and is associated with the spectroscopic line at $f_{02/2} = 4.8$ GHz. Also, at $\varphi_e \approx 0.75\pi$ and $\varphi_e \approx 1.25\pi$ there are regimes when the first three energy levels are equidistant and are the pivot points in the anharmonicity sign. The atom with zero anharmonicity for the first two transitions [31] ($|0\rangle \rightarrow |1\rangle$ and $|1\rangle \rightarrow |2\rangle$), which is intermediate between a two-level system (TLS) and a harmonic oscillator, may find interesting applications in the generation of nonclassical light [32]. All extracted parameters from the fits are summarized in Table I. The potentials $U(\varphi)$ are very similar to each other for the qubits under study. We operate in a single well, very similar to the transmon regime but confined to the nonperiodic potential ($E_J \sim E_L$) (see insets in Fig. 10 in Appendix F). The extracted parameters are also used to make predictions and test the validity of the theoretical model employed in the analysis. The experimental setup and measurement equipment are described in Appendix C.

The symmetric kinemons (group B) are also characterized using spectroscopic measurements. The kinemon VII transmission and two-tone spectra are presented in Fig. 3(b), where in insets we highlight several distinct features at and near the sweet spots. In the current scheme, we operate in the regime where $E_{J1} = E_{J2}$, leading to zero anharmonicity at the bottom sweet spots ($\alpha^{(b)} = 0$ for $\varphi_e = \pi + 2\pi k$, $k \in \mathbb{Z}$ and does not depend on κ). In other words, the Josephson energy is canceled, when a half

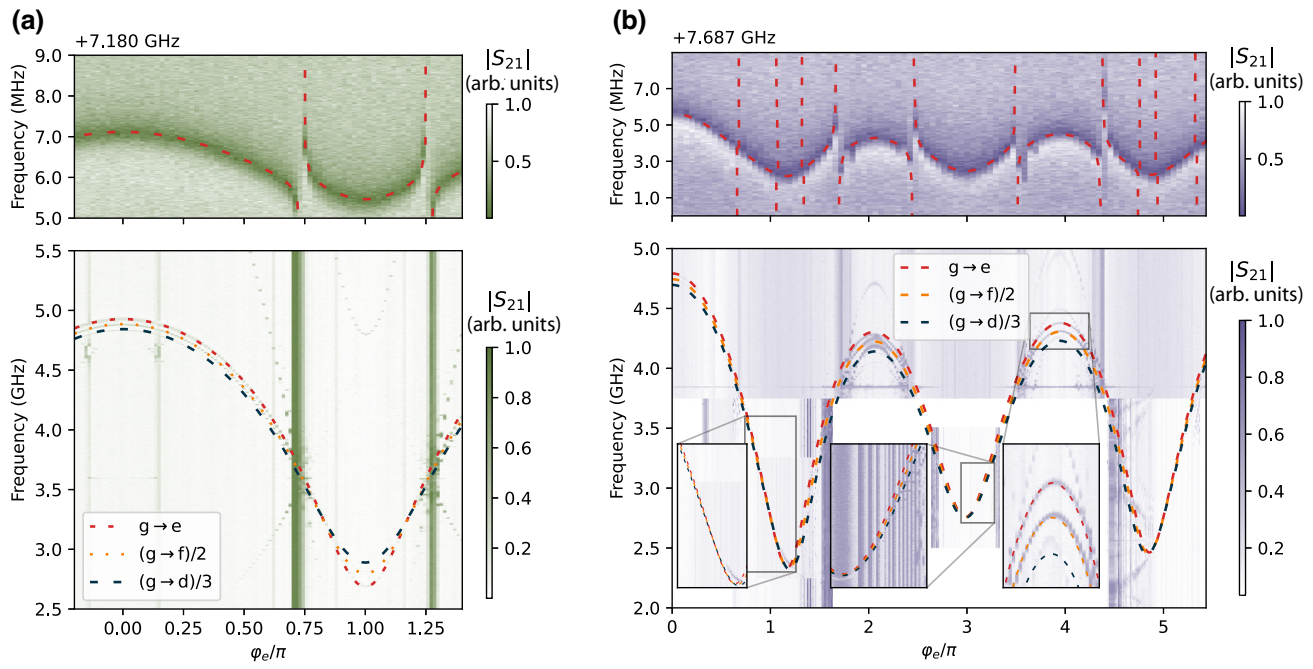


FIG. 3. (a) Kinemon I: (Top) Transmission spectroscopy of the coupled resonator showing feedline frequency response depending on the external flux bias φ_e . (Bottom) Experimental two-tone spectroscopy, displaying the magnitude of the readout signal at a properly chosen readout frequency as a function of flux bias φ_e and kinemon atom excitation frequency. For group A, the anharmonicity sign changes at the $\varphi_e = 0.75\pi$ and gets back at $\varphi_e = 1.25\pi$. Numerical simulation of the spectrum reproducing experimental results with labeled transitions. (b) Kinemon VII: (Top) Transmission spectroscopy of the coupled resonator. (Bottom) Experimental two-tone spectroscopy, with insets (middle and right) showing magnifications at the bottom and top flux sweet spots. For group B, the regimes of harmonic oscillator are noticeable near $\varphi_e = \pi + 2\pi k$, $k \in \mathbb{Z}$ (left and middle inset), while at $\varphi_e \approx 1.15\pi$ only the three lowest levels are equidistant and shown in the left inset.

flux quantum Φ_0 penetrates through the SQUID, causing a transition into the harmonic regime. In our model, the fitting was based solely on the Hamiltonian for a qubit as given in Eq. (1), excluding the qubit-resonator coupling. This likely resulted in the observed deviations, which are visible on the insets. While this approach may compromise some accuracy, it sufficiently captures the essential

qubit parameters; the visibility of higher-order transitions is due to high-power pump signals emphasizing multiphoton transitions. The modulation of the frequency at the top sweet spots corresponds to the nonidentical areas of the SQUIDs. By fitting the spectrum, we evaluate κ to 0.35 and 0.37 for kinemons VII and VIII, respectively, which is in a good agreement with the design areas. We

TABLE I. Kinemons parameters extracted by fitting. Coherence times are given at $\varphi_e = 0$.

	I	II	III	IV	V	VI	VII	VIII
E_J/h , GHz	5.01	6.00	4.00	2.92	2.44	5.90	8.61	14.00
E_C/h , GHz	0.99	1.10	1.50	1.95	1.80	0.70	0.47	0.32
E_L/h , GHz	7.78	8.75	7.40	8.40	9.07	14.65	8.11	12.20
E_J/E_C	5.06	5.45	2.67	1.50	1.36	8.43	18.32	43.75
E_L/E_C	7.86	7.95	4.93	4.31	5.04	20.93	17.26	38.13
E_J/E_L	0.64	0.69	0.54	0.35	0.27	0.40	1.06	1.15
$\omega_{01}^{(t)}/2\pi$, GHz	4.947	5.596	5.719	6.508	6.359	5.312	4.769	5.008
$\omega_r/2\pi$, GHz	7.185	7.284	7.341	7.433	7.495	7.608	7.688	7.779
$g_s/2\pi$, MHz	64	44	34	35	34	90	83	68
$\alpha^{(t)}/h$, MHz	-86	-118	-131	-116	-87	-49	-84	-80
$\alpha^{(b)}/h$, MHz	219	301	257	182	124	96	-	-
T_1 , μ s	17.92 ± 0.95	17.56 ± 0.86	19.45 ± 1.62	8.95 ± 0.33	8.61 ± 0.29	20.39 ± 0.93	19.18 ± 0.78	14.83 ± 0.87
T_2 , μ s	11.45 ± 0.95	17.30 ± 1.65	11.63 ± 1.20	7.80 ± 0.85	9.69 ± 0.42	13.98 ± 0.75	6.59 ± 0.30	12.28 ± 0.65
T_{2E} , μ s	7.92 ± 2.35	20.84 ± 1.11	...	8.05 ± 0.83	14.87 ± 0.56	18.25 ± 1.06	12.73 ± 0.50	13.32 ± 1.02

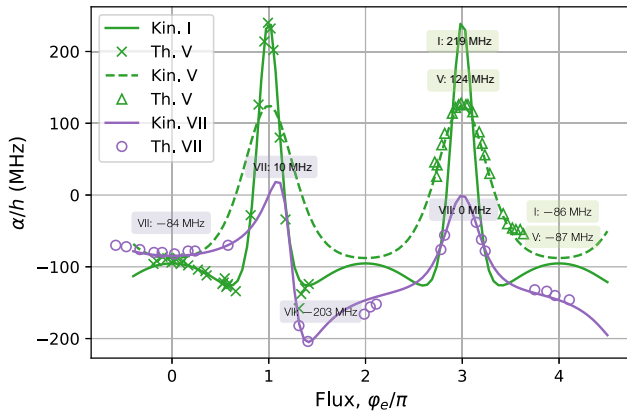


FIG. 4. Anharmonicity as a function of the external flux bias φ_e . The solid line represents theoretical predictions, while crosses, triangles, and circles correspond to the experimental data for kinemon I, V, and VII, respectively. For kinemons I and V, a zero anharmonicity implies that the first three energy levels are equidistant. As for kinemon VII, the anharmonicity becomes exactly zero at $\varphi_e = \pi + 2\pi k$, $k \in \mathbb{Z}$ as it transitions into the harmonic regime, while at $\varphi_e \approx 1.15\pi$ the behavior is similar to group A.

have calculated the areas of both loops and found approximately $S_1 = 230 \mu\text{m}^2$ and $S_2 = 320 \mu\text{m}^2$, which correlates well with the observed nonidentical fluxes resulting in $\kappa = S_1/(S_1 + S_2) \approx 0.4$. These values determine the locations of nonperiodic spots of three-level equidistance (similar to group A) at $\varphi_e \approx 1.15\pi$ and $\varphi_e \approx 4.9\pi$, respectively.

To illustrate better the behavior of the spectra, we plot the anharmonicity of the kinemons I, V, and VII versus the magnetic flux in Fig. 4. For all devices, we calculate the anharmonicity as $\alpha/h = 2 \times (f_{02}/2 - f_{01})$. For kinemon I this yields $\alpha^{(t)}/h = -86 \text{ MHz}$ and $\alpha^{(b)}/h = 219 \text{ MHz}$ for the top and bottom sweet spots, respectively. Kinemon V shows a lower peak anharmonicity, but overall demonstrates a flatter dependence on φ_e due to an increased E_C value. For kinemon VII, zero anharmonicity at $\varphi_e = \pi + 2\pi k$, $k \in \mathbb{Z}$ is associated with a transition into a harmonic oscillator; the additional feature at $\varphi_e \approx 1.15\pi$ mirrors the effect observed in kinemons I and V, corresponding to the three-level equidistance. For the higher-level transitions the harmonic behavior remains the same (see Fig. 8 in Appendix D). Interestingly, for this qubit the anharmonicity is mostly negative and is higher in absolute value in the top sweet spot near $\varphi_e = 2\pi$ than at $\varphi_e = 0$. Another peculiarity is that due to the nontrivial κ dependence of the potential, one can find a sign change of anharmonicity at $\varphi_e = \pi + 2\pi k$, $k \in \mathbb{Z}$. However, if the flux is simultaneously near one of the other sets of special points $\varphi_e/\pi = (1 + 2k')/(2\kappa - 1)$, $k' \in \mathbb{Z}$ (for our case, this is near $\varphi_e \approx 3\pi$, $k' = -1$), the sign of α remains the same.

Finally, we analyze the energy-relaxation time T_1 , the Ramsey coherence time T_2 , and the echo coherence time

T_2^E (see in Table I). The experimental results for kinemon VI are presented in Fig. 5, which provides a comparative analysis of relaxation times under two distinct flux-bias conditions, specifically at $\varphi_e = 0$ (represented in navy color) and $\varphi_e = \pi$ (represented in red color). Corresponding measurement protocols are presented on each subplot. We also measure the coherence outside the sweet spot at most flux-sensitive points and find the lowest characteristic times to be about 600 and 200 ns for T_2^E and T_2 , respectively; the reduction is probably caused by the flux noise due to the insufficient filtering. The relaxation time remains the same with respect to the flux value. The experimental data for T_1 are presented in the top-left subplot. At the top sweet spot, a specific value noted as $20.39 \pm 0.93 \mu\text{s}$. The values represented by triangles on the red line seem slightly higher than at $\varphi_e = 0$, indicating a slower relaxation rate at $\varphi_e = \pi$ with a particular time noted as $23.74 \pm 0.85 \mu\text{s}$. The echo coherence time is plotted in the bottom-left subplot, with measurement results of $18.25 \pm 1.06 \mu\text{s}$ and $19.28 \pm 0.50 \mu\text{s}$ at flux biases of $\varphi_e = 0$ and $\varphi_e = \pi$, respectively. The Ramsey coherence times are presented in the remaining subplot and yield $13.98 \pm 0.75 \mu\text{s}$ and $14.53 \pm 0.35 \mu\text{s}$ at both sweet spots, respectively. Also, additional measurements of conventional transmons fabricated with the same technological process give about 14, 8, and 9 μs for T_1 , T_2 , T_2^E , respectively; however, observed performance improvement of kinemons could be caused by differences between the measurement setups.

The use of low-loss material, such as ultrathin aluminum-film inductors, not only improves device scalability but also enhances performance compared to other materials [21,33,34]. These observations indicate that the shunting capacitance may be further reduced to make the kinemon design even more compact compared to the transmons. For example, the typical value of $E_c = 1.5 \text{ GHz}$ for transmons [35,36] could be increased up to 5–6 GHz with corresponding anharmonicity at the bottom sweet spot $\alpha^{(b)} \approx 2 \text{ GHz}$ for kinemons and will scale down the capacitors, which is promising for the scalability of multiqubit systems (see Fig. 10 in Appendix F). By incorporating a nonzero inductive term in the Hamiltonian, we reduce the sensitivity to charge induced on the electrode, leading to a decreased $\partial E_{ge}/\partial n_g$. This in turn helps to mitigate dephasing arising from charge or electric field fluctuations, predominantly from the dielectric substrate, setting it apart from the transmon with identical parameters. Additionally, the advantage of having a sign-changing anharmonicity attracts interest in waveguide quantum optics [37], for example, allowing pairs of correlated photons to be emitted [38] and nonlinear intermodulation processes to be observed [39] or could help to optimize gate errors caused by a parasitic partial CPHASE operation induced by high-order coupling [40,41], or be useful for new regimes of Bose-Hubbard model simulators [42,43].

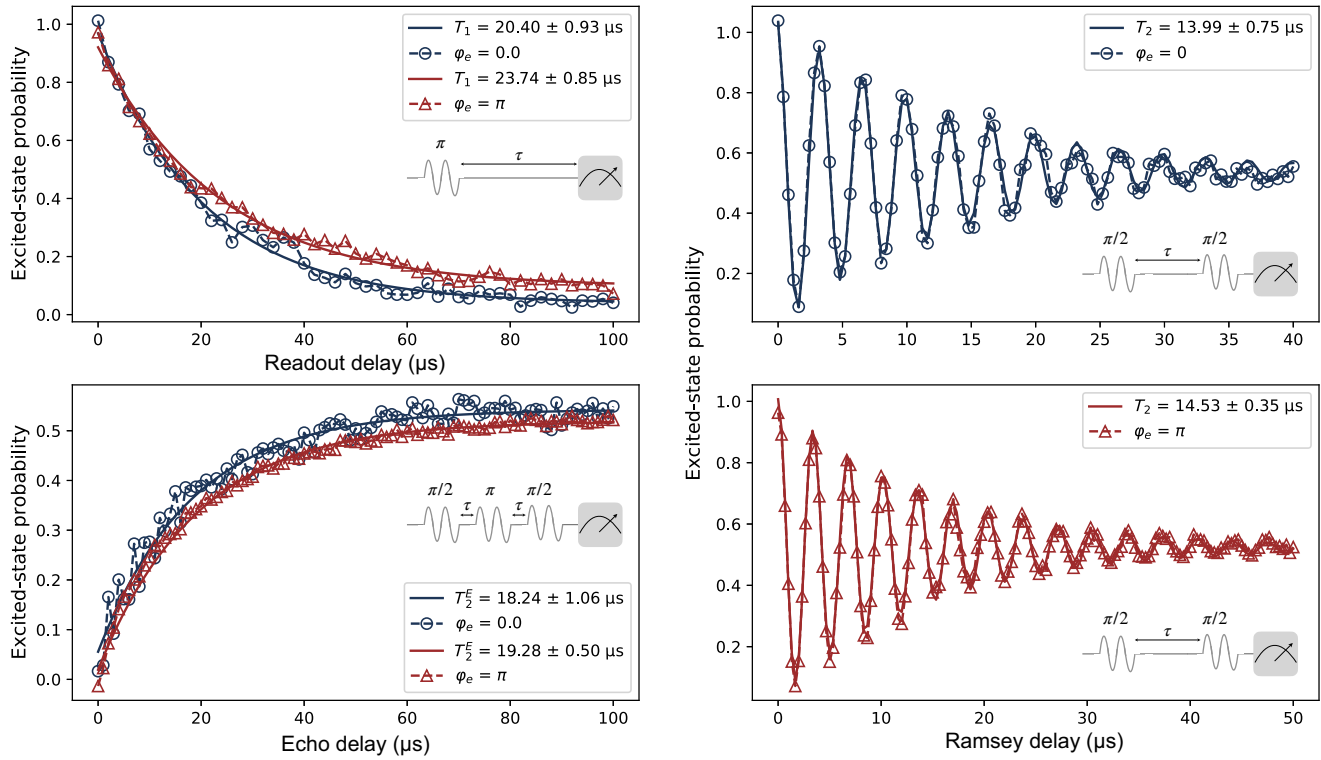


FIG. 5. Energy relaxation and coherence times for kinemon VI measured at different flux bias. The analysis considers two flux bias conditions, $\varphi_e = 0$ (navy circles) and $\varphi_e = \pi$ (red triangles). The top-left subplot reveals the T_1 time at the top sweet spot, demonstrating stability with a value of $20.39 \pm 0.93 \mu\text{s}$. Triangles on the red line represent higher T_1 values, $23.74 \pm 0.85 \mu\text{s}$, suggesting slower relaxation at $\varphi_e = \pi$. The echo coherence time (T_2^E) is depicted in the bottom left subplot. Measurements display times of $18.25 \pm 1.06 \mu\text{s}$ and $19.28 \pm 0.50 \mu\text{s}$ for $\varphi_e = 0$ and $\varphi_e = \pi$, respectively. Lastly, the remaining subplot illustrates Ramsey coherence times (T_2), yielding values of $13.98 \pm 0.75 \mu\text{s}$ and $14.53 \pm 0.35 \mu\text{s}$ at the respective sweet spots.

In conclusion, this study demonstrates that inductively shunted transmon qubits, utilizing ultra-thin aluminum-film inductors, provide a promising platform for scalable quantum computing applications. To increase anharmonicity and strike a balance between high anharmonicity and low charge-noise sensitivity, a reduction in capacitance should be considered. Thus, introducing a nonzero kinetic inductance component can address this issue. While this study represents a significant step towards realizing large-scale, practical quantum computing systems, further research is required to fully explore and validate the potential of this approach in the field of quantum computing.

The raw data that support the findings of this study are available on a reasonable request from the corresponding author.

ACKNOWLEDGMENTS

The authors are grateful to Russian Science Foundation Project Grant No. 21-42-00025 for financial support. The sample was fabricated using equipment of MIPT Shared Facilities Center.

APPENDIX A: DESIGN OF THE QUBIT SAMPLES

A layer-by-layer design was generated using the Klayout-python library [44], which automates the design of superconducting quantum circuits. This library utilizes the KLayout layout design program API and enables the execution of arbitrary Python code through an embedded interpreter. The library specializes in designing microwave and superconducting qubit planar designs, including drawing patterns, simulation, and domain-specific design rule checkers.

APPENDIX B: DEVICE FABRICATION

The device fabrication steps consist of five main stages: ground-plane construction, nanofabrication of Josephson junction and kinetic wire, bandage deposition, and air-bridge construction.

We start with silicon-substrate treatment, which includes piranha etching and BHF dipping [45,46]. The substrate is then immediately placed in the Plassys e-beam evaporation system, and a 100-nm 99.999% aluminum film is evaporated. The metallized substrate is spin coated

with optical resist AZ1517. The coplanar waveguide feedline, resonators, qubit capacitors, and ground-plane hole array are patterned using a laser maskless optical lithography system, followed by dry etching of the optical resist mask structure in BCl_3/Cl_2 inductively coupled plasma. Residual resist is then removed in N-methyl-2-pyrrolidone (NMP) and cleaned in O_2 plasma.

The next step includes hard-mask preparation [47]. The substrate is spin coated with polymer resist PMGI SF9. Then, a 30-nm tungsten nanolayer is deposited in a Torr magnetron sputtering system, followed by ARP-04 resist coating. Josephson junctions are patterned by electron lithography and evaporated using the Dolan bridge technique [48], followed by liftoff in NMP. To form the tunnel barrier, the first 25-nm aluminum junction electrode is oxidized at 40 mBar. Then, a 45-nm electrode is evaporated and preventively oxidized at 10 mBar. Residual resist is removed in NMP and cleaned in O_2 plasma.

The kinetic part is fabricated during an additional cycle of e-beam lithography. We use a single layer of ARP-04 e-beam resist to construct the pattern. After development, an 8-nm aluminum film is evaporated at the Plassys stage temperature of 170 K at a normal angle. Residual resist is then removed in NMP and cleaned in O_2 plasma.

Good galvanic contact between the layers is obtained by aluminum bandages [49]. We use a similar process of single-layer mask as for the kinetic part above, but without cooling. A 150-nm aluminum film is evaporated with *in situ* Ar ion milling. Residual resist is removed during the liftoff process in NMP and cleaned in O_2 plasma.

Due to the presence of coplanar lines on the ground plane, we need to achieve a uniform electrical potential; therefore, the final stage of sample fabrication is the implementation of aluminum free-standing air bridges [50]. A 7- μm layer of SPR220 photoresist is spin coated, and the base layer is patterned using a laser maskless optical lithography system. After development, the substrate is heated to create a height gradient on the resist edges, followed by a 600-nm aluminum evaporation with *in situ* Ar ion etching. A second layer of SPR220 photoresist is used to form a bridge structure. Finally, the excess metal is dry etched in BCl_3/Cl_2 inductively coupled plasma. Residual resist is then removed in NMP and cleaned in O_2 plasma.

APPENDIX C: MICROWAVE EXPERIMENTAL SETUP

The device under investigation is measured in a dilution refrigerator at 10 mK (Fig. 6). Signals are generated using an arbitrary waveform generator (Keysight M3202A) and rf synthesizers (SignalCore 5502A), followed by up-conversion in *IQ* mixers (Marki IQ4509 and IQ0307). Excitation and dispersive readout signals are combined using a directional coupler and sent to the fridge, where they are attenuated by 60 dB to reduce thermal

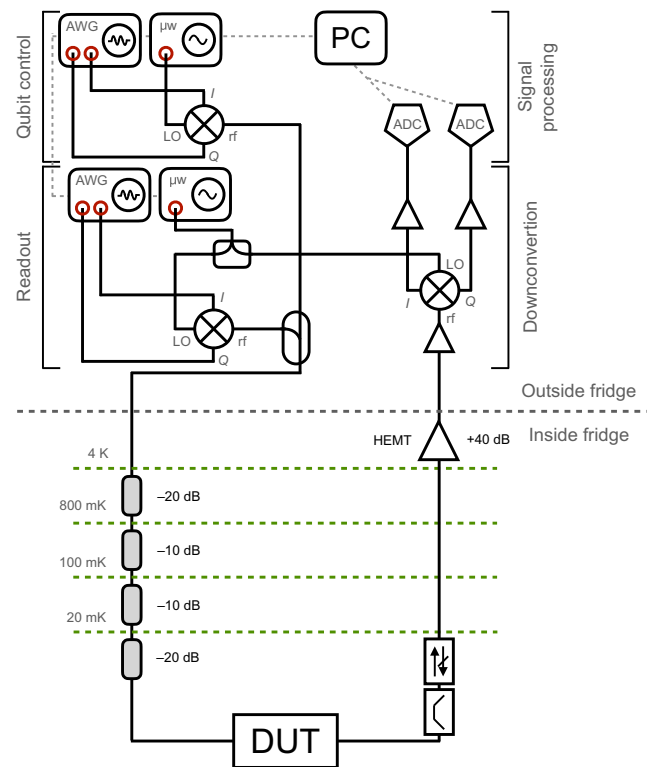


FIG. 6. Schematic of experimental setup to measure the sample depicting room-temperature equipment and line configuration inside the BlueFors dilution refrigerator, with the base temperature of 10 mK.

noise reaching the sample. The response from the readout resonators located on the sample is amplified using a HEMT and room-temperature amplifiers. Finally, the readout signal is down-converted and digitized at a 100-MHz IF frequency using a Spectrum Instruments m4x PXI card. Using this scheme, qubit spectra are obtained under continuous excitation and readout. Artificial atoms' coherence times are characterized using conventional time-domain techniques [3,51].

APPENDIX D: ANHARMONICITY OF HIGHER TRANSITIONS

APPENDIX E: CAVITY COUPLING

To plot the model curves describing the dependence of the resonator frequency on the magnetic flux (the upper panels of Fig. 3), we solve the following Hamiltonian in the φ basis for the kinemon and in the Fock basis for the cavity:

$$\hat{\mathcal{H}}_{\text{QED}} = \hat{\mathcal{H}} + \hbar\omega_r(\hat{a}^\dagger\hat{a} + 1/2) + \hbar g(\hat{a}^\dagger - \hat{a}) \otimes \frac{\partial}{\partial\varphi},$$

where $\hat{\mathcal{H}}$ is defined by Eq. (1), \hat{a} is the bosonic annihilation operator, and the capacitive coupling term is derived

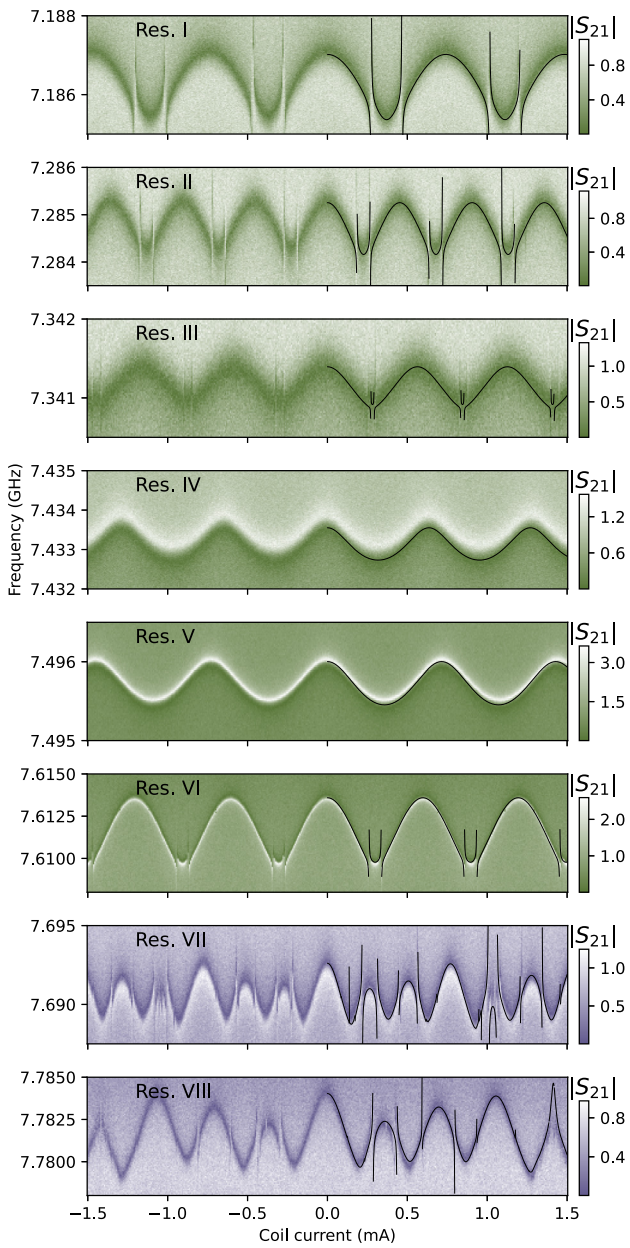


FIG. 7. Transmission spectroscopy for all resonators coupled to kinemons with varying energy ratios. $|S_{21}|$ includes the attenuation and amplification in the measurement chain. Avoided crossings occur when a qubit's $|0\rangle \rightarrow |2\rangle$ transition (or even higher levels for kinemons VII and VIII) intersects with its readout cavity frequency. Some very sharp avoided crossings are just barely resolved in the simulations. Also, some of the predicted features are smeared in experiment due to the power-broadening effects (located around 1.1 mA for VII and 1.4 mA for VIII).

using the canonical quantization expression for the \hat{n} operator, $[\hat{n}, \hat{\varphi}] = i$. The corresponding coupling coefficient g is defined by fitting the model to the data.

For numerical solution of the stationary Schrödinger equation for $\hat{\mathcal{H}}_{\text{cQED}}$, we use separate finite difference

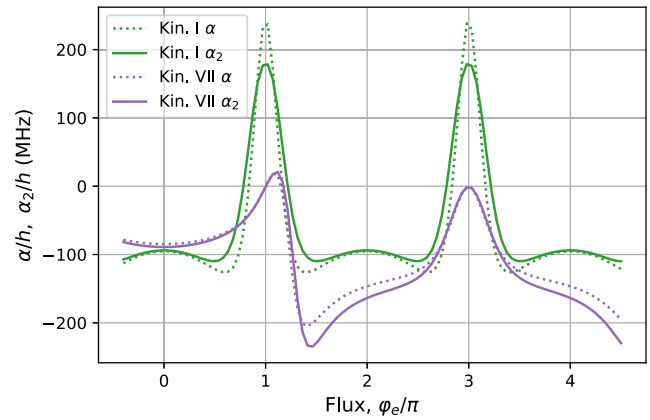


FIG. 8. Comparison of higher-level transition anharmonicity ($\alpha_2/h = E_{23} - E_{12}$) and anharmonicity ($\alpha/h = E_{12} - E_{01}$) as a function of external flux bias (φ_e) for kinemons I and VII is presented. Kinemon VII maintains the harmonic regime at higher levels when $\varphi_e = \pi + 2\pi k$, $k \in \mathbb{Z}$, while for kinemon I α differs.

formulas of the sixth order to approximate the first and the second derivatives. This allows convergence of the necessary low-lying eigenenergies to be achieved on a rough φ grid of 30 to 50 nodes, which then facilitates execution of the computationally demanding fitting algorithms.

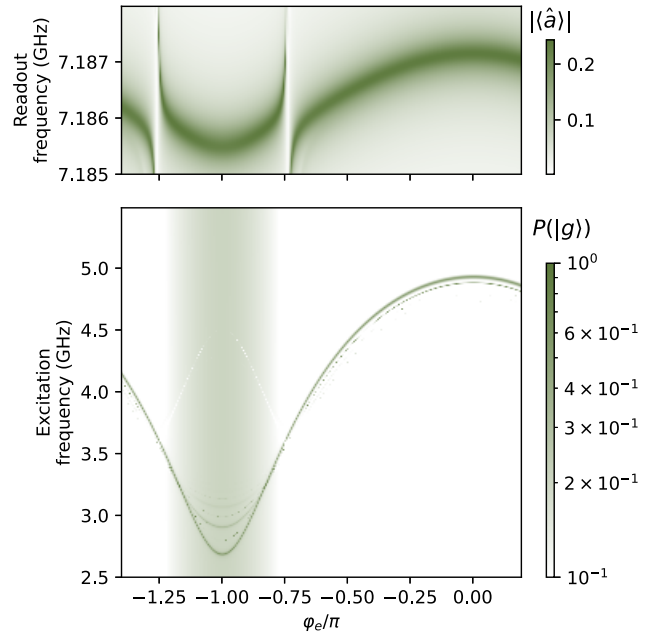


FIG. 9. Simulated spectra for the kinemon I, obtained from the master equation solution. Color shows the expectation value of the cavity field $|\langle \hat{a} \rangle|$ (top) and the depopulation of the ground state, $1 - P(|g\rangle)$, (bottom). Simulation parameters: $\Omega/2\pi = 200$ MHz for the kinemon spectrum (= 0.1 MHz for the cavity spectrum), $\omega_r/2\pi = 7.1851$ GHz, $g/2\pi = 64$ MHz, $\kappa = 2.5 \mu\text{s}^{-1}$, $\gamma = 10 \mu\text{s}^{-1}$.

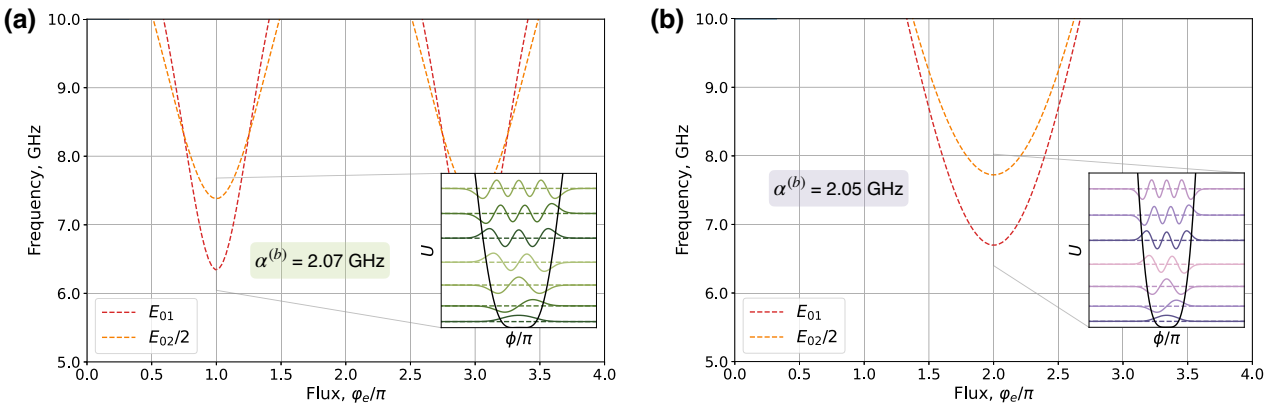


FIG. 10. (a) Calculated spectrum of the optimized single-junction kinemon (group A) near the lower sweet spot and the corresponding eigenstates for the parameters $E_C/h = 10.00 \text{ GHz}$, $E_J/h = 5.00 \text{ GHz}$, $E_L/h = 4.50 \text{ GHz}$. (b) Calculated spectrum of the optimized double-junction kinemon (group B) near the lower sweet spot and the corresponding eigenstates for the parameters $E_C/h = 5.00 \text{ GHz}$, $E_{J1}/h = 9.00 \text{ GHz}$, $E_{J2}/h = 7.00 \text{ GHz}$, $E_L/h = 16.00 \text{ GHz}$.

To reproduce the multiphoton transitions, which can be observed in the lower panels of Fig. 3, we also perform a time-domain simulation by solving the GKSL equation based on the $\hat{\mathcal{H}}_{\text{cQED}}$ -defined unitary evolution and dissipative energy-relaxation dynamics characterized by the collapse operators $\sqrt{\kappa}\hat{a}$ and $\sqrt{\gamma}\hat{b}$, κ, γ being the corresponding decay rates. Here, the kinemon lowering operator \hat{b} for each value of φ_e is constructed from the lowest eigenstates $|E_n\rangle$,

$$\hat{b} = \hat{1}_r \otimes \sum_n |E_n\rangle \langle E_{n+1}|.$$

Then, at a given φ_e , the master equation is solved with an addition of a resonator driving term to $\hat{\mathcal{H}}_{\text{cQED}}$ of the form $\hbar\Omega(\hat{a}^\dagger + \hat{a})\cos\omega_d t$. The driving frequency $\omega_d/2\pi$ is scanned through the same range that is used in the spectroscopy, i.e., from 2.5 to 5.5 GHz, and the resulting steady-state density matrices are saved for further calculation of the observables.

We show the results for both the transmission spectroscopy and the two-tone spectroscopy in Fig. 9. We note overall a good agreement with the experimental data, but find an extra spectral line in Fig. 3(a), having its minimum at around 4.7 GHz, which is not reproduced in the simulation. We attribute it to a sideband two-photon process taking one thermal photon from the cavity and exciting the kinemon to its fourth excited state located around 12 GHz above the ground state at the lower sweet spot (in the modeling, the cavity is at zero temperature, so such a process cannot be observed). The upside-down-looking spectral line having a maximum frequency of 4.5 GHz is a vice versa process, depopulating the kinemon from $|e\rangle$ to $|g\rangle$ and exciting the cavity. It is observable in the simulation as $|e\rangle$ is slightly populated for $\varphi \in [-1.2, -0.8]$ due to the numerical errors.

APPENDIX F: OPERATION MODES OF KINEMONS

In our current work, we have selected the $E_J/E_L/E_C$ parameters to develop a family of proof-of-concept devices that is compatible with typical experimental setup constraints. All of the qubits operate within a single well potential (insets in Fig. 10). This operational characteristic primarily stems from the relatively high value of E_L (Fig. 1) that we have employed. As a result, the wave function of the qubits is strongly confined around the minimum of the potential well, mirroring the behavior typically seen in transmon qubits.

In future research, we plan to investigate devices featuring higher E_C values while maintaining them within the transmon frequency range. For example, for kinemon qubits of the second type (group B) with optimized E_C value set to 5 GHz, the corresponding E_{J1} , E_{J2} , and E_L values can be chosen to be 9, 7, and 16 GHz, respectively, to fulfill the frequency condition ($\kappa = 0.5$). This choice results in the anharmonicity of approximately +2 GHz at the lower sweet spot (the only parking spot). We demonstrate the numerical spectrum (the main and the two-photon transitions) and the potential landscape associated with these parameters in Fig. 10(b). It can be seen, though, that the anharmonicity drops quickly with the detuning from the parking spot, so this type of kinemon will probably be most useful in the fixed-frequency regime with tunable couplers to perform two-qubit gates. Likewise, group A can be utilized similarly, featuring a single bottom sweet spot and positive α , resulting in an anharmonicity of $\alpha^{(b)} = +2.07 \text{ GHz}$, as illustrated in Fig. 10(a).

[1] J. Koch, T. M. Yu, J. Gambetta, A. A. Houck, D. I. Schuster, J. Majer, A. Blais, M. H. Devoret, S. M. Girvin, and

- R. J. Schoelkopf, Charge-insensitive qubit design derived from the Cooper pair box, *Phys. Rev. A* **76**, 042319 (2007).
- [2] J. A. Schreier, A. A. Houck, J. Koch, D. I. Schuster, B. R. Johnson, J. M. Chow, J. M. Gambetta, J. Majer, L. Frunzio, M. H. Devoret, S. M. Girvin, and R. J. Schoelkopf, Suppressing charge noise decoherence in superconducting charge qubits, *Phys. Rev. B* **77**, 180502 (2008).
- [3] P. Krantz, M. Kjaergaard, F. Yan, T. P. Orlando, S. Gustavsson, and W. D. Oliver, A quantum engineer's guide to superconducting qubits, *Appl. Phys. Rev.* **6**, 021318 (2019).
- [4] J. J. Burnett, A. Bengtsson, M. Scigliuzzo, D. Nipce, M. Kudra, P. Delsing, and J. Bylander, Decoherence benchmarking of superconducting qubits, *npj Quantum Inf.* **5**, 54 (2019).
- [5] R. Schutjens, F. A. Dagga, D. J. Egger, and F. K. Wilhelm, Single-qubit gates in frequency-crowded transmon systems, *Phys. Rev. A* **88**, 052330 (2013).
- [6] V. Vesterinen, O. P. Saira, A. Bruno, and L. DiCarlo, Mitigating information leakage in a crowded spectrum of weakly anharmonic qubits, *arXiv:1405.0450* (2014).
- [7] Z. Chen, *et al.*, Measuring and suppressing quantum state leakage in a superconducting qubit, *Phys. Rev. Lett.* **116**, 020501 (2016).
- [8] M. McEwen, *et al.*, Removing leakage-induced correlated errors in superconducting quantum error correction, *Nat. Commun.* **12**, 1761 (2021).
- [9] C. C. Bultink, T. E. O'Brien, R. Vollmer, N. Muthusubramanian, M. W. Beekman, M. A. Rol, X. Fu, B. Tarasinski, V. Ostroukh, B. Varbanov, A. Bruno, and L. DiCarlo, Protecting quantum entanglement from leakage and qubit errors via repetitive parity measurements, *Sci. Adv.* **6**, eaay3050 (2020).
- [10] K. C. Miao, *et al.*, Overcoming leakage in scalable quantum error correction, *arXiv:2211.04728 [quant-ph]* (2022).
- [11] T. Roy, Z. Li, E. Kapit, and D. I. Schuster, Realization of two-qutrit quantum algorithms on a programmable superconducting processor, *arXiv:2211.06523 [quant-ph]* (2022).
- [12] I. V. Pechenezhskiy, R. A. Mencia, L. B. Nguyen, Y.-H. Lin, and V. E. Manucharyan, The superconducting quasicharge qubit, *Nature* **585**, 368 (2020).
- [13] A. Gyenis, P. S. Mundada, A. Di Paolo, T. M. Hazard, X. You, D. I. Schuster, J. Koch, A. Blais, and A. A. Houck, Experimental realization of a protected superconducting circuit derived from the $0-\pi$ qubit, *PRX Quantum* **2**, 010339 (2021).
- [14] H. Zhang, S. Chakram, T. Roy, N. Earnest, Y. Lu, Z. Huang, D. K. Weiss, J. Koch, and D. I. Schuster, Universal fast-flux control of a coherent, low-frequency qubit, *Phys. Rev. X* **11**, 011010 (2021).
- [15] E. Hyypää, *et al.*, Unimon qubit, *Nat. Commun.* **13**, 6895 (2022).
- [16] F. Hassani, M. Peruzzo, L. N. Kapoor, A. Trioni, M. Zemlicka, and J. M. Fink, Inductively shunted transmons exhibit noise insensitive plasmon states and a fluxon decay exceeding 3 hours, *Nat. Commun.* **14**, 3968 (2023).
- [17] T. P. Orlando, J. E. Mooij, L. Tian, C. H. van der Wal, L. S. Levitov, S. Lloyd, and J. J. Mazo, Superconducting persistent-current qubit, *Phys. Rev. B* **60**, 15398 (1999).
- [18] I. Chiorescu, Y. Nakamura, C. J. P. M. Harmans, and J. E. Mooij, Coherent quantum dynamics of a superconducting flux qubit, *Science* **299**, 1869 (2003).
- [19] J. Q. You, X. Hu, S. Ashhab, and F. Nori, Low-decoherence flux qubit, *Phys. Rev. B* **75**, 140515 (2007).
- [20] F. Yan, S. Gustavsson, A. Kamal, J. Birenbaum, A. P. Sears, D. Hover, T. J. Gudmundsen, D. Rosenberg, G. Samach, S. Weber, J. L. Yoder, T. P. Orlando, J. Clarke, A. J. Kerman, and W. D. Oliver, The flux qubit revisited to enhance coherence and reproducibility, *Nat. Commun.* **7**, 12964 (2016).
- [21] J. T. Peltonen, P. C. J. J. Coumou, Z. H. Peng, T. M. Klapwijk, J. S. Tsai, and O. V. Astafiev, Hybrid rf squid qubit based on high kinetic inductance, *Sci. Rep.* **8**, 10033 (2018).
- [22] I. N. Moskalenko, I. A. Simakov, N. N. Abramov, A. A. Grigorev, D. O. Moskalev, A. A. Pishchimova, N. S. Smirnov, E. V. Zikiy, I. A. Rodionov, and I. S. Besedin, High fidelity two-qubit gates on fluxoniums using a tunable coupler, *npj Quantum Inf.* **8**, 130 (2022).
- [23] Y. Nakamura, Y. A. Pashkin, and J. S. Tsai, Coherent control of macroscopic quantum states in a single-cooper-pair box, *Nature* **398**, 786 (1999).
- [24] F. Yan, Y. Sung, P. Krantz, A. Kamal, D. K. Kim, J. L. Yoder, T. P. Orlando, S. Gustavsson, and W. D. Oliver, Engineering framework for optimizing superconducting qubit designs, *arXiv:2006.04130 [quant-ph]* (2020).
- [25] F.-M. Liu, M.-C. Chen, C. Wang, S.-W. Li, Z.-X. Shang, C. Ying, J.-W. Wang, C.-Z. Peng, X. Zhu, C.-Y. Lu, and J.-W. Pan, Quantum design for advanced qubits: Plasmonium, *arXiv:2109.00994 [quant-ph]* (2022).
- [26] F. G. Paauw, A. Fedorov, C. J. P. M. Harmans, and J. E. Mooij, Tuning the gap of a superconducting flux qubit, *Phys. Rev. Lett.* **102**, 090501 (2009).
- [27] D. Kalacheva, G. Fedorov, I. Khrapach, and O. Astafiev, Coplanar superconducting resonators with nonlinear kinetic inductance bridge, *Supercond. Sci. Technol.* **36**, 055011 (2023).
- [28] K. K. Likharev and A. B. Zorin, Theory of the Bloch-wave oscillations in small Josephson junctions, *J. Low Temp. Phys.* **59**, 347 (1985).
- [29] M. H. Devoret, Does Brian Josephson's gauge-invariant phase difference live on a line or a circle? *J. Superconduct. Novel Magnet.* **34**, 1633 (2021).
- [30] G. Fedorov and A. Ustinov, Automated analysis of singletone spectroscopic data for CQED systems, *Quantum Sci. Technol.* **4**, 045009 (2019).
- [31] P. Bardetski and M. Macovei, Cavity steady-state behaviors for a single equidistant three-level emitter, *Phys. Scr.* **67**, 306 (2003).
- [32] S. Gasparinetti, J.-C. Besse, M. Pechal, R. D. Buijs, C. Eichler, H. J. Carmichael, and A. Wallraff, Two-photon resonance fluorescence of a ladder-type atomic system, *Phys. Rev. A* **100**, 033802 (2019).
- [33] P. Winkel, K. Borisov, L. Grünhaupt, D. Rieger, M. Specker, F. Valenti, A. V. Ustinov, W. Wernsdorfer, and I. M. Pop, Implementation of a transmon qubit using superconducting granular aluminum, *Phys. Rev. X* **10**, 031032 (2020).

- [34] D. Rieger, S. Günzler, M. Spiecker, P. Paluch, P. Winkel, L. Hahn, J. Hohmann, A. Bacher, W. Wernsdorfer, and I. Pop, Granular aluminium nanojunction fluxonium qubit, *Nat. Mater.* **22**, 194 (2023).
- [35] J. Stehlík, D. M. Zajac, D. L. Underwood, T. Phung, J. Blair, S. Carnevale, D. Klaus, G. A. Keefe, A. Carniol, M. Kumph, M. Steffen, and O. E. Dial, Tunable coupling architecture for fixed-frequency transmon superconducting qubits, *Phys. Rev. Lett.* **127**, 080505 (2021).
- [36] Google Quantum AI, Suppressing quantum errors by scaling a surface code logical qubit, *Nature* **614**, 676 (2023).
- [37] X. Gu, A. F. Kockum, A. Miranowicz, Y.-x. Liu, and F. Nori, Microwave photonics with superconducting quantum circuits, *Phys. Rep.* **718**, 1 (2017).
- [38] S. Gasparinetti, M. Pechal, J.-C. Besse, M. Mondal, C. Eichler, and A. Wallraff, Correlations and entanglement of microwave photons emitted in a cascade decay, *Phys. Rev. Lett.* **119**, 140504 (2017).
- [39] T. Höngl-Decrinis, I. V. Antonov, R. Shaikhaidarov, V. N. Antonov, A. Y. Dmitriev, and O. V. Astafiev, Mixing of coherent waves in a single three-level artificial atom, *Phys. Rev. A* **98**, 041801 (2018).
- [40] F. Yan, P. Krantz, Y. Sung, M. Kjaergaard, D. L. Campbell, T. P. Orlando, S. Gustavsson, and W. D. Oliver, Tunable coupling scheme for implementing high-fidelity two-qubit gates, *Phys. Rev. Appl.* **10**, 054062 (2018).
- [41] P. Zhao, P. Xu, D. Lan, J. Chu, X. Tan, H. Yu, and Y. Yu, High-contrast zz interaction using superconducting qubits with opposite-sign anharmonicity, *Phys. Rev. Lett.* **125**, 200503 (2020).
- [42] G. Fedorov, S. Remizov, D. Shapiro, W. Pogosov, E. Egorova, I. Tsitsilin, M. Andronik, A. Dobronosova, I. Rodionov, O. Astafiev, *et al.*, Photon transport in a Bose–Hubbard chain of superconducting artificial atoms, *Phys. Rev. Lett.* **126**, 180503 (2021).
- [43] X. Zhang, E. Kim, D. K. Mark, S. Choi, and O. Painter, A superconducting quantum simulator based on a photonic-bandgap metamaterial, *Science* **379**, 278 (2023).
- [44] <https://github.com/shamil777/AQSDesign>.
- [45] A. Bruno, G. de Lange, S. Asaad, K. L. van der Enden, N. K. Langford, and L. DiCarlo, Reducing intrinsic loss in superconducting resonators by surface treatment and deep etching of silicon substrates, *Appl. Phys. Lett.* **106**, 182601 (2015).
- [46] D. Kalacheva, G. Fedorov, A. Kulakova, J. Zotova, E. Korostylev, I. Khrapach, A. V. Ustinov, and O. V. Astafiev, Improving the quality factor of superconducting resonators by post-process surface treatment, *AIP Conf. Proc.* **2241**, 020018 (2020).
- [47] L. Liechao, J. Kang, and J. Wen, Low stress TiN as metal hard mask for advance Cu-interconnect, *ECS Trans.* **44**, 481 (2012).
- [48] G. J. Dolan, Offset masks for lift-off photoprocessing, *Appl. Phys. Lett.* **31**, 337 (1977).
- [49] A. Osman, J. Simon, A. Bengtsson, S. Kosen, P. Krantz, D. P. Lozano, M. Scigliuzzo, P. Delsing, J. Bylander, and A. Fadavi Roudsari, Simplified Josephson-junction fabrication process for reproducibly high-performance superconducting qubits, *Appl. Phys. Lett.* **118**, 064002 (2021).
- [50] Z. Chen, A. Megrant, J. Kelly, R. Barends, J. Bochmann, Y. Chen, B. Chiaro, A. Dunsworth, E. Jeffrey, J. Y. Mutus, P. J. J. O’Malley, C. Neill, P. Roushan, D. Sank, A. Vainsencher, J. Wenner, T. C. White, A. N. Cleland, and J. M. Martinis, Fabrication and characterization of aluminum airbridges for superconducting microwave circuits, *Appl. Phys. Lett.* **104**, 052602 (2014).
- [51] D. I. Schuster, A. Wallraff, A. Blais, L. Frunzio, R.-S. Huang, J. Majer, S. M. Girvin, and R. J. Schoelkopf, ac stark shift and dephasing of a superconducting qubit strongly coupled to a cavity field, *Phys. Rev. Lett.* **94**, 123602 (2005).